

Determination of the Magnetic Structure of Spin Glass Compound $\text{Zn}_{0.5}\text{Mn}_{0.5}\text{Te}$ Using Real-Space Methods

Sabrina R. Hatt,¹ Camille Shaw,¹ Emma Zappala,¹ Raju Baral,^{1,2} Stuart Calder,²
Gerald D. Morris,³ Brenden R. Ortiz,⁴ Karine Chesnel,¹ and Benjamin A. Frandsen¹

¹*Department of Physics and Astronomy, Brigham Young University, Provo, Utah 84602, USA.*

²*Neutron Scattering Division, Oak Ridge National Laboratory, Oak Ridge, Tennessee 37831, USA.*

³*Centre for Molecular and Materials Science, TRIUMF,*

Vancouver, British Columbia, Canada V6T 2A3

⁴*Materials Science and Technology Division, Oak Ridge National Laboratory, Oak Ridge, Tennessee 37831, USA.*

We present a combined magnetometry, muon spin relaxation (μSR), and neutron scattering study of the insulating spin glass $\text{Zn}_{0.5}\text{Mn}_{0.5}\text{Te}$, for which magnetic Mn^{2+} and nonmagnetic Zn^{2+} ions are randomly distributed on a face-centered cubic lattice. Using magnetic pair distribution function (mPDF) analysis and reverse Monte Carlo (RMC) modeling of the diffuse magnetic scattering, we show that the spin-glass ground state exhibits short-range type-III antiferromagnetic order with a locally ordered moment of $3.4 \mu_{\text{B}}$ between nearest-neighbor spins, which decays as a function of spin separation distance with a correlation length of approximately 5 \AA . The diffuse magnetic scattering and corresponding mPDF show no significant changes across the spin-glass freezing temperature $T_f = 22 \text{ K}$, indicating that the dynamically fluctuating short-range spin correlations in the paramagnetic state retain the same basic type-III configuration that characterizes the spin-glass state; the only change apparent from the neutron scattering data is a gradual reduction of the correlation length and locally ordered moment with increasing temperature. The μSR results demonstrate that fluctuation rate of the short-range spin correlations decreases gradually and somewhat inhomogeneously through the sample volume as the temperature decreases toward T_f . Taken together, these results provide a unique and detailed picture of the local magnetic structure and dynamics in a concentrated spin glass. In addition, this work showcases a new statistical method for extracting diffuse scattering signals from neutron powder diffraction data, which we developed to facilitate the mPDF and RMC analysis of the neutron data. This method has the potential to be broadly useful for neutron powder diffraction experiments on a variety of materials with short-range atomic or magnetic order.

INTRODUCTION

A spin glass is a magnetic state in which the magnetic moments are frozen in a disordered configuration, lacking the long-range order typical of conventional magnetic ground states. Such a state can arise in materials that possess magnetic frustration and an element of randomness, e.g. disordered atomic site occupation in an alloy [1]. Upon warming through the spin-glass freezing temperature T_f , the system undergoes a classical phase transition into a paramagnetic state with fluctuating magnetic moments [2]. Despite the lack of long-range magnetic order in spin glasses, the magnetic moments nevertheless exhibit short-range correlations as dictated by the magnetic interactions governing the system, and these correlations may persist dynamically above T_f [1]. Questions about the nature of the spin-glass phase transition have stimulated a vast amount of theoretical and experimental research for over five decades and continue even now [1–5], earning spin glasses a prominent place within condensed matter physics. Indeed, the importance of spin glasses extends well beyond the bounds of traditional condensed matter physics: as a paradigm of complexity, concepts developed in the study of spin glasses have seen application to topics as wide-ranging as protein dynamics, neural networks, combinatorial optimization, and more [6].

Experimental probes that are sensitive to local magnetic correlations in the absence of long-range order are crucial for studying spin glasses. Two such probes that have been highly influential in spin-glass studies are muon spin relaxation/rotation (μSR), in which spin-polarized muons implanted in the sample interact with the local magnetic field they experience, and neutron scattering, which probes the two-spin correlation function in the material. The short-range magnetic correlations in a spin glass produce a diffuse neutron scattering pattern that encodes information about the local magnetic structure.

During the nascent stages of the spin-glass field, crucial advances were enabled by both μSR and neutron scattering [1, 7, 8]. In the decades since these seminal early works, technical capabilities for μSR and especially neutron scattering have advanced tremendously, providing data with much greater sensitivity and accuracy than was previously possible [9, 10]. For example, increased neutron flux, more widespread use of spin-polarized neutrons, higher energy resolution, and more sophisticated computational modeling capabilities have revolutionized neutron scattering studies of magnetic materials.

The transformative capabilities of modern experimentation and data analysis invite a renewed look into spin glasses, both classic systems from decades past as well as newer systems of interest. A handful of recent

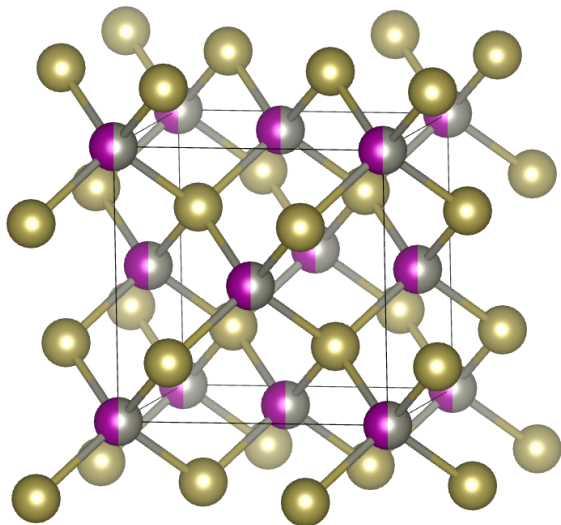


FIG. 1. Structure of $\text{Zn}_{0.5}\text{Mn}_{0.5}\text{Te}$, generated in VESTA [19]. The lattice exhibits a zincblende structure composed of two interlaced FCC lattices, one containing only Te atoms (gold) and the other with 50% each occupancy of Zn and Mn (violet and silver).

neutron-scattering studies of spin glasses highlight the unprecedented level of detail that can be achieved, such as directionally-resolved magnetic correlation lengths in anisotropic systems [11], precise determination of magnetic cluster sizes [12], and subtle differences between static versus dynamic spin correlations across the freezing temperature [13, 14].

In this work, we revisit the spin-glass compound $\text{Zn}_{0.5}\text{Mn}_{0.5}\text{Te}$, which is a model system for dense, insulating spin glasses with short-range interactions between local magnetic moments [15–18]. $\text{Zn}_{0.5}\text{Mn}_{0.5}\text{Te}$ crystallizes in the zincblende structure, as shown in Fig. 1, with the Zn^{2+} and Mn^{2+} ions randomly occupying the positions of a face-centered cubic (fcc) lattice. The freezing temperature for $(\text{Zn},\text{Mn})\text{Te}$ can be tuned by adjusting the Zn:Mn ratio; for $\text{Zn}_{0.5}\text{Mn}_{0.5}\text{Te}$, $T_f = 22$ K. Earlier neutron diffraction studies revealed a broad distribution of diffuse intensity centered around $(1, 1/2, 0)$ and similar positions in reciprocal space, which was suggested to result from incipient type-III antiferromagnetic ordering [15]. Qualitatively similar diffuse scattering patterns were observed above T_f , indicating that dynamic short-range magnetic correlations survive in the paramagnetic state with the same overall spatial modulation observed in the frozen state.

Our approach for extracting information about the local spin correlations from the neutron scattering data is to use the magnetic pair distribution function (mPDF) [20, 21], which entails computing the Fourier transform of the magnetic scattering pattern to yield the spin-pair correlation function directly in real space. The successful use of the Fourier transform of diffuse magnetic scattering to study spin glasses has been demon-

strated in the past [22–25], but these earlier studies were mainly limited to qualitative or semi-quantitative analysis and often suffered from marginal data quality. Only over the last 10 years has a complete formalism of mPDF analysis been developed [26], enabling a more quantitative treatment of Fourier-transformed diffuse scattering data. Together with major improvements in neutron instrumentation and data quality, these developments have enabled successful mPDF studies of short-range magnetism in systems ranging from geometrically frustrated quantum magnets [27–30] to magnetically enhanced thermoelectrics [31, 32] to spin glasses [12, 33]. We complement the real-space mPDF analysis with additional analysis in reciprocal space using the reverse Monte Carlo (RMC) method to fit supercell spin configurations to the scattering data [34, 35].

Here, we combine neutron scattering data on $\text{Zn}_{0.5}\text{Mn}_{0.5}\text{Te}$ with dc magnetometry and μSR data collected over a wide temperature range to provide a highly detailed view of the evolution of the local magnetic correlations in $\text{Zn}_{0.5}\text{Mn}_{0.5}\text{Te}$ from deep within the spin-glass state up to room temperature. Key results include confirmation of short-range type-III antiferromagnetic ordering, quantitative refinement of the locally ordered magnetic moment and magnetic correlation length as a function of temperature, measurement of the homogeneity of the spin-freezing process throughout the sample, and clear evidence that the instantaneous local magnetic structure undergoes no significant change across T_f . In addition, we describe a data processing method that effectively separates the diffuse magnetic scattering signal from the sharp nuclear Bragg peaks, enabling reliable mPDF analysis of data collected from a neutron powder diffractometer not specifically designed for conventional PDF analysis. The results shed new light on this class of spin-glass systems and demonstrate the effectiveness of this methodological approach for studying spin glasses and other systems with short-range magnetic order.

METHODS

Sample Synthesis

Stoichiometric amounts of Zn powder (99.9%), Mn powder (99.95%), and Te pieces (99.999%) were mixed thoroughly with an agate mortar and pestle inside an argon glovebox and sealed in an evacuated quartz ampoule. The ampoule was heated to 700 °C and held there for 24 hours. The sample was then removed from the ampoule, ground in an agate mortar and pestle, sealed once again in an evacuated quartz ampoule, and annealed again at 700 °C for 24 hours. Four samples of approximately 1 g each were prepared in this way and combined into a single sample to be used for subsequent experimentation.

Bulk Structural and Magnetic Characterization

The sample structure and purity were quantified via laboratory X-ray diffraction (XRD) using a PANalytical X'Pert Pro reflection geometry powder XRD instrument, and the resulting data were analyzed by Rietveld refinement using PANalytical's High Score Plus software [36]. The bulk magnetic behavior was characterized with a superconducting quantum interference device (SQUID) magnetometer (Quantum Design MPMS-3). Measurements were made in a warming sequence between 1.8 K and 300 K under zero-field-cooled (ZFC) and field-cooled (FC) conditions with an applied field of 1000 Oe.

Muon Spin Relaxation

In a μ SR experiment, spin-polarized positive muons with a mean lifetime of about 2.2 μ s are implanted in a sample, and their decay into positrons is monitored as a function of time after implantation. The decay positron is emitted preferentially in the direction of the muon spin at the moment of decay. The experimental quantity of interest is the time-dependent μ SR asymmetry, which is the normalized difference in positron counts between two detectors placed on opposite sides of the sample as a function of time after muon implantation. This quantity is proportional to the muon ensemble spin polarization projected along the axis defined by the two detectors [37]. As a probe of the local magnetic environment, μ SR is sensitive both to long-range and short-range magnetic correlations and can distinguish between sample volumes that exhibit static magnetism versus paramagnetism. In addition, μ SR can probe magnetic relaxation times between approximately 10^{-5} and 10^{-11} s, which is situated nicely between the slower time-scale sensitivity of SQUID magnetometry and the faster sensitivity of neutron diffraction [37].

μ SR experiments were performed at TRIUMF Lab-

oratory using the LAMPF spectrometer on endstation M20D. A 500-mg portion of the powder sample used for the neutron diffraction experiment was pressed into a pellet of diameter approximately 1 cm for use in the μ SR experiment. The temperature was controlled using a helium gas flow cryostat with a base temperature of 1.9 K. Helmholtz coils were used to generate a uniform magnetic field at the sample position, with a maximum applied field of 0.4 T. The μ SR spectra were analyzed using the open-source software BEAMS [38].

Neutron Diffraction Experiment and Data Analysis

Neutron Diffraction Experiment

Neutron diffraction measurements were performed on the HB2A powder diffractometer at Oak Ridge National Laboratory's High Flux Isotope Reactor (HFIR) facility. The sample was loaded into a vanadium sample can and mounted in a helium cryostat. Diffraction patterns were collected in a warming sequence at 3 K, 15, 28, 40, 100, 150, 225, and 295 K for 6 hours each. The neutron wavelength used was 1.54 \AA , yielding a maximum momentum transfer Q of approximately 8 \AA^{-1} . At 3 K, an additional diffraction pattern was collected with a neutron wavelength of 1.12 \AA^{-1} , yielding a maximum Q of about 10 \AA^{-1} .

Magnetic PDF Analysis

Magnetic PDF data were obtained via Fourier transformation of the Q -dependent diffuse magnetic scattering cross section. The procedure to separate the magnetic scattering from the nuclear scattering is described in detail in the Results section. Two variants of the mPDF were utilized in this study. The first, which we call the deconvolved or normalized mPDF, is given by [20, 39]

$$G_{\text{mag}}(r) = \frac{2}{\pi} \int_{Q_{\text{min}}}^{\infty} Q \left(\frac{(\text{d}\sigma/\text{d}\Omega)_{\text{mag}}}{\frac{2}{3}N_s S(S+1)(\gamma r_0)^2 [f_m(Q)]^2} - 1 \right) \sin(Qr) \text{d}Q \quad (1)$$

$$= \frac{3}{2S(S+1)} \left(\frac{1}{N_s} \sum_{i \neq j} \left[\frac{A_{ij}}{r} \delta(r - r_{ij}) + B_{ij} \frac{r}{r_{ij}^3} \Theta(r_{ij} - r) \right] - 4\pi r \rho_0 \frac{2}{3} m^2 \right). \quad (2)$$

Eq. 1 provides the experimental definition of the mPDF, while Eq. 2 is how the mPDF is calculated for a given configuration of spins. In these equations, Q_{min} is the minimum momentum transfer included in the Fourier transform (assumed to exclude the small-angle scattering

regime), $(\text{d}\sigma/\text{d}\Omega)_{\text{mag}}$ is the magnetic differential scattering cross section, r is the distance in real space, $r_0 = \frac{\mu_0}{4\pi} \frac{e^2}{m_e}$ is the classical electron radius, $\gamma = 1.913$ is the neutron magnetic moment in units of nuclear magnetons, S is the spin quantum number in units of \hbar , $f_m(Q)$

is the magnetic form factor, N_s is the number of spins in the system, i and j label individual spins \mathbf{S}_i and \mathbf{S}_j separated by the distance r_{ij} , and A_{ij} and B_{ij} are spin orientation coefficients as described in [20]. In addition, Θ is the Heaviside step function, m is the average magnetic moment in Bohr magnetons (which is zero for anything with no net magnetization, such as antiferromagnets), and ρ_0 is the number of spins per unit volume. We refer to it as the deconvolved mPDF because division by $[f_m(Q)]^2$ in Eq. 1 effectively deconvolves the real-space mPDF from the effect of the Q -space damping of the magnetic intensity caused by the magnetic form factor.

The other mPDF variant used, which we refer to as the non-deconvolved or unnormalized mPDF, is given by [21]

$$d_{\text{mag}}(r) = \frac{2}{\pi} \int_{Q_{\text{min}}}^{\infty} Q \left(\frac{d\sigma}{d\Omega} \right)_{\text{mag}} \sin(Qr) dQ \quad (3)$$

$$= C_1 \times G_{\text{mag}}(r) * S(r) + C_2 \times \frac{dS}{dr}, \quad (4)$$

where C_1 and C_2 are constants, $*$ represents the convolution operation, and $S(r) = \mathcal{F}\{f_m(Q)\} * \mathcal{F}\{f_m(Q)\}$ (where \mathcal{F} denotes the Fourier transform). The second term on the right of Eq. 4 comes from the self-scattering contribution to the magnetic differential scattering cross section and results in a peak at low r below approximately 1 Å. As seen from the equations, the non-deconvolved mPDF d_{mag} is essentially the deconvolved mPDF G_{mag} convolved twice with the Fourier transform of the magnetic form factor. As a result, it has reduced resolution in real space, so it is advantageous to use G_{mag} when the quality of the scattering data is high enough. In practice, division by $[f(Q)]^2$ can introduce significant errors into the Fourier transform for noisy scattering data, in which case the non-deconvolved mPDF may be preferable.

The experimental mPDF patterns were produced by the `diffpy.mpdf` software [40] using the procedure described in Ref. [32]. Both the deconvolved and non-deconvolved mPDF patterns were produced for the data collected at 3 K; for all other temperatures, only the non-deconvolved mPDF patterns were used. In all cases, we used $Q_{\text{max}} = 4.5 \text{ \AA}^{-1}$. Fits to the mPDF data were performed using `diffpy.mpdf`. The fitting parameters included a scale factor that controls the amplitude of the mPDF and is related to the locally ordered magnetic moment [41], the angles describing the overall orientation of the magnetic configuration relative to the crystal axes, and the finite correlation length governing the extent of the short-range magnetic order.

Reverse Monte Carlo Modeling

We performed additional analysis of the neutron scattering data in reciprocal space using reverse Monte Carlo (RMC) modeling as implemented in `Spinvert` [42]. In

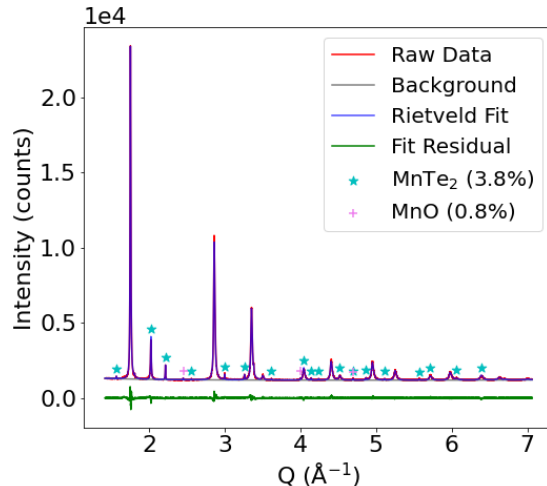


FIG. 2. Rietveld refinement of X-ray diffraction (XRD) data.

this approach, the orientations of magnetic moments in a large supercell are randomly adjusted until they produce a simulated scattering pattern that is consistent with the data. Considering that the RMC method utilizes reciprocal-space data and does not require a starting guess for the magnetic structure, this method is complementary to the model-dependent real-space mPDF method.

From the RMC-generated spin configurations, the spin correlation function can be calculated as

$$\langle \mathbf{S}(0) \cdot \mathbf{S}(r) \rangle = \frac{1}{N} \sum_{i=1}^N \sum_{j=1}^{Z_i(r)} \frac{\mathbf{S}_i \cdot \mathbf{S}_j}{\langle Z_i(r) \rangle}, \quad (5)$$

where each magnetic moment is represented as \mathbf{S}_i , $\langle Z_i(r) \rangle$ is the average coordination number for a distance r from the central magnetic moment, and N is the total number of magnetic moments in the supercell. `Spinvert` can be run multiple times to produce several fits. Then the spin correlation function can be calculated and averaged over all fits to give the best result. This function can be used to help visualize the relative orientation of correlated magnetic moments, thus helping to deduce the structure.

RESULTS

XRD and Magnetometry

The powder XRD pattern of the sample at room temperature is shown in Fig. 2. The main $\text{Zn}_{0.5}\text{Mn}_{0.5}\text{Te}$ phase with the expected cubic structure accounts for 95% of the molar fraction of the sample. The refined lattice parameter is 6.2150(5) Å. Based on an earlier compositional study of the (Zn,Mn)Te system [43], this lattice parameter corresponds to 48% Mn concentration,

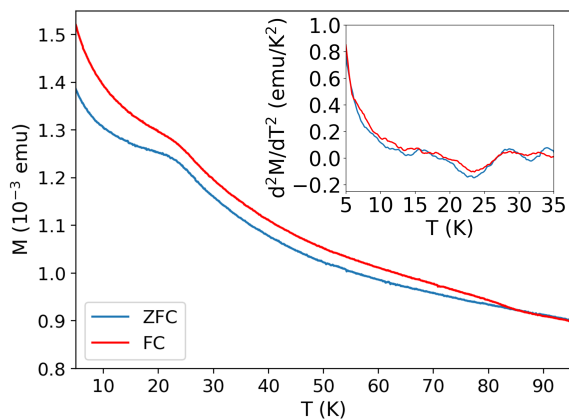


FIG. 3. Field cooled (red) and zero-field cooled (blue) magnetization, gathered by superconducting quantum interference device (SQUID) magnetometry. Data were collected in a warming sequence. Inset: Second derivative of magnetization.

which is close to the 50% composition we targeted in the synthesis. We also identified two minor impurity phases: MnTe_2 at 3.8% and MnO at 1%.

We display the dc magnetometry data in Fig. 3. The data were collected in a warming sequence. The two most notable features are a kink around 21–23 K and a merging of the ZFC and FC curves around 85 K. The kink agrees closely with the previously reported freezing temperature of 21 K for a very similar composition [18]. The transition is also quite clear in the second derivative of the magnetization (inset of Fig. 3), confirming that our sample undergoes the expected spin-glass transition at low temperature. Based on the finite width of the kink in the magnetization, we estimate the freezing temperature of our sample to be $T_f = 22(1)$ K. We attribute the ZFC and FC branching around 85 K to the impurity phase MnTe_2 , which has an antiferromagnetic ordering temperature of 86.5 K [44]. The overall increase of the magnetization with decreasing temperature appears somewhat more pronounced than previously published data [18], suggesting that dilute paramagnetic impurities in the sample may contribute to this effect. Fortunately, the XRD and magnetometry both confirm the expected behavior in the majority $\text{Zn}_{0.5}\text{Mn}_{0.5}\text{Te}$ phase, affirming the suitability of this sample for detailed studies of the local magnetic correlations using neutron diffraction and μSR .

Muon Spin Relaxation

To characterize the spin-glass transition more fully, we performed μSR measurements of $\text{Zn}_{0.5}\text{Mn}_{0.5}\text{Te}$ at several temperatures between 2 K and ~ 90 K. The μSR asymmetry spectra collected in zero applied field (ZF) are shown in Fig. 4(a). The spectra collected between 56.2 K and 87.6 K are similar, with only slightly faster

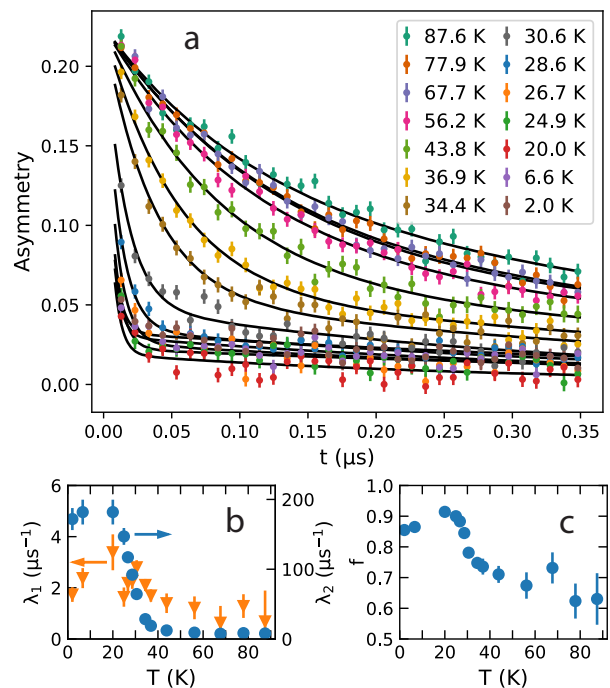


FIG. 4. (a) Zero-field μSR asymmetry spectra for $\text{Zn}_{0.5}\text{Mn}_{0.5}\text{Te}$ collected between 2 K and 87.6 K. Colored symbols represent the experimental data, solid curves the fits using Eq. 6. (b) Temperature dependence of the slow relaxation rate λ_1 (left vertical axis, orange triangles) and fast relaxation rate λ_2 (right vertical axis, blue circles) extracted from fits to the ZF spectra. (c) Temperature dependence of the spectral weight f of the fast-relaxing component.

relaxation evident for 56.2 K compared to 87.6 K. This type of relaxation is consistent with fluctuating spins in the paramagnetic state. As the temperature decreases to 43.8 K and below, the asymmetry develops a fast front end with very rapid relaxation. For 20.0 K and below, the spectra are nearly indistinguishable, with the fast front end fully relaxing within $0.05 \mu\text{s}$ and the longer-time tail remaining relatively constant with time. The fast front end is expected for a local spin configuration that is highly disordered but quasi-static on the muon timescale [45], i.e. fluctuations slower than approximately 0.1 MHz. To confirm that the rapid relaxation at early times is due to static magnetism, we performed a series of μSR measurements in an applied longitudinal field (LF, not shown) up to 0.4 T, in which we observed significant recovery (i.e. decoupling) of the asymmetry with increasing LF. Furthermore, the large fraction of the total asymmetry undergoing the rapid front-end relaxation confirms that the transition occurs throughout the full sample volume.

Qualitatively, then, the μSR data shown in Fig. 4(a) indicate that the freezing transition as observed on the muon timescale occurs in the temperature range ~ 24 - 44 K. This can be quantified more rigorously through least-squares fits to the ZF asymmetry spectra. We

found that the spectra can be accurately described using the two-component asymmetry function

$$a(t) = a_0 [(1 - f)e^{-\lambda_1 t} + fe^{-\lambda_2 t}], \quad (6)$$

where $a_0 = 0.225$ is the total initial asymmetry at $t = 0$, λ_1 and λ_2 are slow and fast relaxation rates, respectively, and f is the fractional weight of the fast-relaxing component. The best-fit values of λ_1 , λ_2 , and f are shown in Fig. 4(b,c). The beginning of the transition around 44 K is evident in the rapid increase in the λ_2 and f below this temperature, corresponding to the appearance of the fast front end in the spectra and signifying the freezing of spins on the muon timescale. The freezing process occurs gradually throughout the sample volume between 44 K and 24 K, as demonstrated by the gradual increase of f in this temperature range. That the transition region is at a higher temperature as observed by μ SR compared to dc magnetometry can be explained by the fact that μ SR is sensitive to spin fluctuations on a faster timescale than dc magnetometry, so fluctuations just above T_f are slow enough to appear static for μ SR but still dynamic for magnetometry. We note that similar behavior has been observed in μ SR data collected on magnetic nanoparticles exhibiting superparamagnetism [46], suggesting a qualitative analogy between the spin dynamics at the atomic scale in spin glasses and the dynamics of the collective nanoparticle magnetic moment at the nanoscale in magnetic nanoparticles.

Notably, the asymmetry spectra collected above 44 K still require two exponential components for a satisfactory fit. This is counter to expectations for the case of uncorrelated spin fluctuations in a conventional paramagnet, where a single exponentially relaxing component should fully describe the asymmetry [45], suggesting that nontrivial dynamic spin correlations persist beyond at least 90 K. This is confirmed by neutron diffraction, as discussed in the next section.

Neutron Diffraction

Neutron diffraction probes spin-pair correlations directly, providing an opportunity to gain detailed knowledge of the local magnetic structure of $\text{Zn}_{0.5}\text{Mn}_{0.5}\text{Te}$. In Fig. 5, we display representative neutron powder diffraction patterns collected at several temperatures. In addition to the sharp nuclear Bragg peaks from the crystal structure of $\text{Zn}_{0.5}\text{Mn}_{0.5}\text{Te}$, a broad hump of diffuse scattering centered around 1.1 \AA^{-1} is clearly visible at low temperature, indicative of short-range spin correlations in the spin-glass state. A few sharp Bragg peaks that disappear at higher temperature are also present at low Q (marked by * and +), but based on their positions and temperature dependence, these can be identified as AFM peaks from the MnTe_2 [44] and MnO [47] impurities. Returning to the diffuse scattering feature, we note that with increasing temperature, the diffuse hump becomes

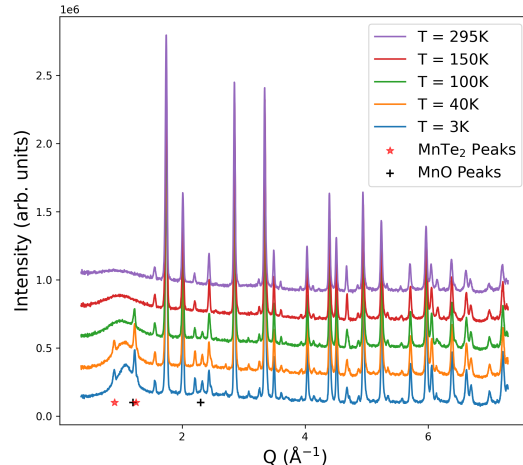


FIG. 5. Representative neutron powder diffraction patterns for $\text{Zn}_{0.5}\text{Mn}_{0.5}\text{Te}$ at various temperatures spanning the spin-glass freezing temperature $T_f = 22 \text{ K}$ (only visually distinct data sets shown). A prominent hump of diffuse magnetic scattering is visible around 1.1 \AA^{-1} , which persists in diminished form to the highest temperature measured. The asterisks and plus signs mark magnetic Bragg peaks from the MnTe_2 and MnO impurity phases, respectively.

both weaker in amplitude and broader. This indicates a lower overall level of orientational correlations between spins and a shorter correlation length. However, this evolution occurs gradually, with no drastic changes evident at or near $T_f = 22 \text{ K}$. Importantly, the neutron diffraction patterns represent the energy-integrated differential scattering cross section, which probes the *instantaneous* (rather than time-averaged) spin correlations in the material. Thus, the persistence of magnetic diffuse scattering well above T_f demonstrates that dynamically correlated spin fluctuations remain in the paramagnetic state but are time-averaged away to zero by slower probes such as magnetometry. This is likewise consistent with the μ SR data.

Data Treatment to Isolate Diffuse Magnetic Scattering

To gain deeper insights into the local magnetic structure of $\text{Zn}_{0.5}\text{Mn}_{0.5}\text{Te}$ through mPDF analysis and RMC modeling, it is necessary to separate the magnetic contributions to the neutron scattering data from the nuclear contributions. One way to accomplish this is to compute the Fourier transform of the nuclear and magnetic scattering data together, which produces the total PDF, i.e. the sum of the atomic and magnetic PDF patterns. The atomic PDF can then be fit to the data and subtracted, leaving only the mPDF. This works well when the accessible Q -range of the measurement is large enough to produce an atomic PDF signal that can be modeled in a meaningful way. In our case using 1.54 \AA neutrons on

HB2A, the diffraction patterns extend only to 8 \AA^{-1} . This is adequate for mPDF data, since the magnetic form factor typically suppresses any meaningful signal beyond this value, but it is insufficient for generating the atomic PDF. If the total PDF were generated using this data, the truncation artifacts would be too severe to allow proper removal of the atomic PDF. The shorter wavelength options at HB2A provide a larger Q -range such that this real-space separation of the nuclear and magnetic signals can be accomplished [48], and we found some success with this approach using the single data set collected at 3 K with 1.12 \AA neutrons (see Supplementary Information). However, the rest of the data collected with the longer wavelength option (which tends to yield a cleaner magnetic signal) require a different treatment.

For the longer-wavelength data, we found more success by separating the magnetic and nuclear signals in Q space rather than real space. To accomplish this, we assumed that the observed diffuse scattering arises solely from the short-range spin correlations in $\text{Zn}_{0.5}\text{Mn}_{0.5}\text{Te}$. This presupposes that $\text{Zn}_{0.5}\text{Mn}_{0.5}\text{Te}$ possesses no chemical short-range ordering that would also cause diffuse scattering, which was previously demonstrated to be a reliable assumption based on the structure and temperature dependence of the diffuse scattering [15]. We further assumed that any diffuse magnetic scattering from the impurity phases MnTe_2 and MnO above their respective Néel temperatures is negligible. Considering that the molar fraction of these combined impurity phases is below 5%, we consider this to be reasonable. The task is then to remove all Bragg peaks from the data, leaving just the diffuse scattering for subsequent analysis in Q space and/or Fourier transformation into the real-space mPDF.

If it is possible to collect a diffraction pattern in the purely paramagnetic state, such that the spin orientations are completely random and no structured diffuse scattering exists, then this high-temperature pattern can be subtracted from the lower-temperature patterns to remove the (ideally) temperature-independent nuclear Bragg peaks and isolate the temperature-dependent diffuse magnetic scattering signal. In our case, even the highest-temperature data set contains appreciable diffuse magnetic scattering, so a straight subtraction would not work. Significant shifts in the peak positions due to thermal expansion would also present challenges for this method, as would the presence of the impurity magnetic Bragg peaks at low temperature.

To circumvent these challenges, we implemented a novel algorithm to detect and remove Bragg peaks automatically from powder data sets, leaving only the diffuse scattering. In this algorithm, the standard deviation of the scattered intensity is computed within a sliding window that passes continuously through the entire data range, yielding an array of standard deviations as a function of Q . Peaks are then identified as regions of

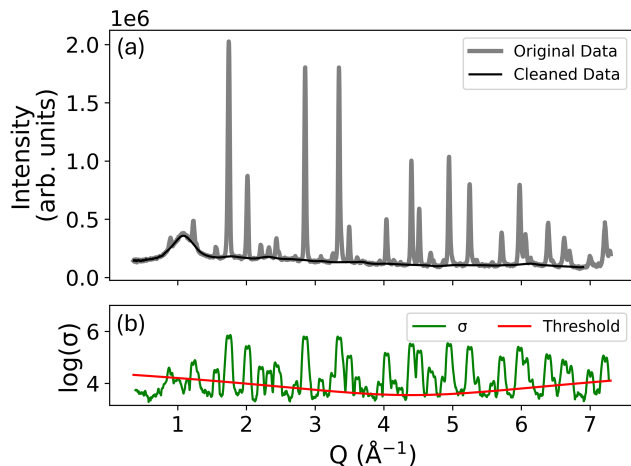


FIG. 6. Extraction of the diffuse scattering signal from the diffraction pattern. (a) Cleaned data overlaid on raw (background subtracted) data. (b) Logarithm of the standard deviation, overlaid by the threshold used to determine the position of peaks, as explained in the main text.

standard deviation above a user-defined threshold. All regions exceeding the threshold are excised from the original scattering pattern, and linear interpolation is used to fill the resulting gaps. The resulting diffuse scattering pattern is somewhat choppy, so convolution with a narrow Gaussian is used to remove abrupt kinks near peak edges. For the case of $\text{Zn}_{0.5}\text{Mn}_{0.5}\text{Te}$, we chose the width of the window for computing the standard deviation to be 0.056 \AA^{-1} after some trial and error. Further, we found that it was suboptimal to use a constant threshold for identifying peaks, because the standard deviation within the diffuse scattering region was larger than that of some of the small Bragg peaks in the mid- Q range. To account for this, we defined the threshold as a shallow quadratic function, which effectively selected the diffuse scattering over the whole Q range.

The result of applying this algorithm to the $\text{Zn}_{0.5}\text{Mn}_{0.5}\text{Te}$ data collected at 3 K is shown in Fig. 6. The algorithm successfully removed all Bragg peaks, leaving a relatively clean diffuse scattering signal suitable for further analysis, including RMC modeling in Q space and mPDF analysis in real space after Fourier transformation. The algorithm was similarly effective for diffraction patterns collected at all other temperatures. We note that excessive peak overlap in the scattering pattern could pose challenges for this algorithm, but considering the high symmetry of $\text{Zn}_{0.5}\text{Mn}_{0.5}\text{Te}$, it was not an obstacle here. Finally, we mention that our python implementation of this algorithm also includes an option to add any magnetic Bragg peaks selected by the user back into the scattering pattern after their initial removal. We did not use this feature in the current study, since no magnetic Bragg peaks exist for $\text{Zn}_{0.5}\text{Mn}_{0.5}\text{Te}$, but it could potentially be useful for situations of coex-

isting magnetic Bragg peaks and magnetic diffuse scattering.

Magnetic PDF analysis

To continue our analysis of the short-range magnetic correlations in $\text{Zn}_{0.5}\text{Mn}_{0.5}\text{Te}$, we now turn to the mPDF, which we generated for each temperature by Fourier transforming the isolated diffuse magnetic scattering. The blue curve in Fig. 7 shows the mPDF at 3 K, labeled as G_{mag} and deconvolved from the effect of the magnetic form factor for improved real-space resolution. The local magnetic structure is immediately evident in the mPDF pattern. We observe a large, negative peak at the nearest neighbor distance of ≈ 4.4 Å, indicative of strong antiferromagnetic nearest-neighbor correlations. The peaks below this distance are truncation artifacts from the Fourier transform. Two positive peaks are visible at distances of approximately 6.2 Å and 7.6 Å, corresponding to net parallel alignment of second- and third-nearest neighbors. Negative as well as positive peaks continue to appear at further interatomic distances, reflective of the net antiferromagnetic local spin arrangement. The magnitudes of these peaks diminish steadily with increasing r , demonstrating the short-range-ordered nature of the spin-glass state and indicating that non-random spin correlations persist on the length scale of about 2-3 nm at 3 K.

We performed a more quantitative analysis of the mPDF data by fitting various magnetic structure models to the data. Most antiferromagnets with the fcc structure exhibit one of a few collinear magnetic configurations, often referred to as types I, II, and III [49]. We modeled the data with each of these three structures, using least-squares optimization to refine a correlation length, the spin direction, and a scale factor set by the magnitude of the locally ordered magnetic moment at the nearest-neighbor distance. Only the type-III order (illustrated in the inset of Fig. 7) provided a reasonable fit to the data, shown as the red curve in Fig. 7. This result confirms a previous prediction of short-range type-III order in this class of materials [15], while also providing greater detail than is available from earlier studies. Specifically, we found that the local magnetic order parameter at the nearest-neighbor distance is $3.4(3) \mu_{\text{B}}$, which dies off exponentially with distance as $\exp(-r/\xi)$ with the correlation length $\xi = 5.7(1)$ Å. The magnitude of the local magnetic order parameter was determined by comparison to the atomic PDF scale factor for the data collected with 1.12 Å neutrons, as explained in the Supplementary Information. The best-fit spin direction is approximately along the propagation vector, similar to the classic type-III fcc antiferromagnet MnS_2 [50]. Taken together, the mPDF fit results paint an exceptionally detailed picture of the local magnetic structure that characterizes the spin-glass ground state in $\text{Zn}_{0.5}\text{Mn}_{0.5}\text{Te}$.

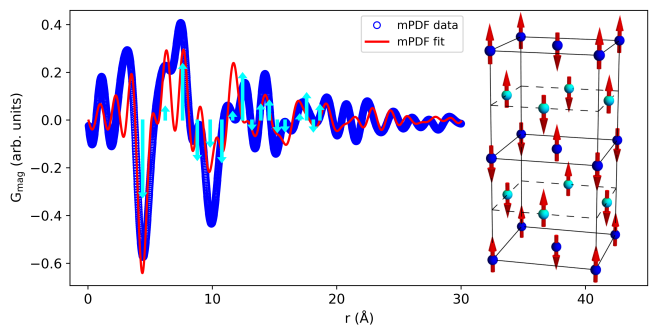


FIG. 7. Fit of antiferromagnetic type-III structure to experimental deconvolved magnetic pair distribution function (mPDF) for $\text{Zn}_{0.5}\text{Mn}_{0.5}\text{Te}$ at 3 K. The average correlation function (calculated over 100 Spinvert fits) is shown as cyan arrows overlaid on the data. Inset: Antiferromagnetic type-III order, with the propagation vector along the vertical axis.

We performed similar fits to the mPDF data collected at all other temperatures, as well. Due to the weaker diffuse scattering signal at higher temperatures, attempting to deconvolve the diffuse scattering from the magnetic form factor prior to Fourier transformation led to untenable levels of noise and Fourier artifacts in the data. Accordingly, we opted instead to use the non-deconvolved mPDF data, which we label d_{mag} . This has the advantage of reducing the noise in the mPDF data, but at the cost of reduced real-space resolution. Fig. 8 shows representative d_{mag} data and fits. We note that the large positive peak below 1 Å is unrelated to any spin-spin correlations and is simply a byproduct of the procedure used to generate the non-deconvolved mPDF, as explained elsewhere [21]. The fit at 3 K is quite good and yields similar results as the fit to the deconvolved mPDF G_{mag} at that temperature, except the correlation length refines to $4.1(1)$ Å, somewhat shorter than the value obtained from the G_{mag} fit. This may be due to the broadening of weak mPDF features at longer r such that they are indistinguishable from the background, shortening the r -range over which meaningful signal exists relative to the deconvolved G_{mag} . Nevertheless, important information can be gleaned from the mPDF data displayed in Fig. 8. First, the mPDF remains qualitatively unchanged between 3 K and 40 K, indicating that the instantaneous local magnetic structure does not undergo a significant change across T_f . Second, the amplitude of the mPDF decreases with increasing temperature, pointing to increased randomness between neighboring spins and a reduction in the local magnetic order parameter. Third, the r -range over which meaningful oscillations in the mPDF signal exist becomes successively shorter with increasing temperature, indicating that the magnetic correlation length decreases. At 295 K, only a slight negative dip around the nearest-neighbor distance is visible, indicating that nearest-neighbor antiferromagnetic correlations persist at room temperature but do not extend to further distances. This analysis is consistent

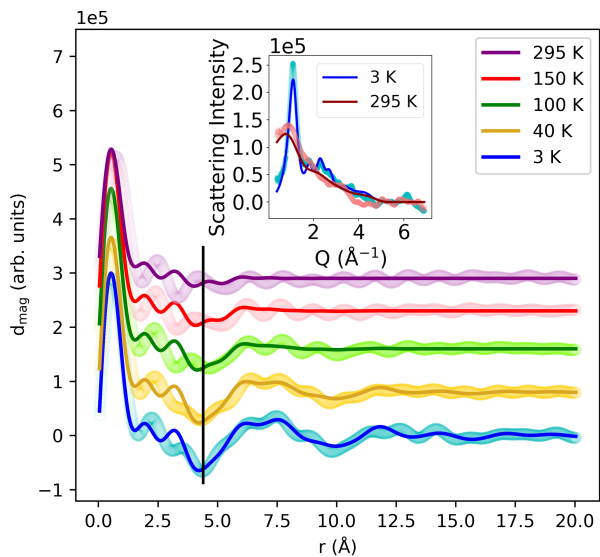


FIG. 8. Non-deconvolved mPDF d_{mag} at representative temperatures between 3 K and 295 K (same temperatures shown in Fig. 5), offset vertically for clarity. Fits using the antiferromagnetic type-III model are overlaid as the darker solid curves. The solid vertical line indicates the nearest neighbor distance, below which Fourier artifacts often accumulate. The inset shows the calculated magnetic scattering corresponding to the mPDF fits at 3 K and 295 K (solid curves) compared to the observed diffuse magnetic scattering (open circles).

with the diffuse magnetic scattering pattern observed at 295 K, displayed in the inset of Fig. 8 along with the diffuse scattering at 3 K for comparison. The best-fit correlation length and local magnetic order parameter values for each temperature are displayed in Fig. 9, confirming the downward trend with temperature inferred from qualitative inspection of the data.

Reverse Monte Carlo Modeling

We next present RMC fits to the diffuse magnetic scattering data at 3 K. As a model-free approach to fitting the data in reciprocal space, this is a valuable independent check of our model-dependent mPDF fits in real space. We defined a $6 \times 6 \times 6$ supercell and performed 100 RMC refinements to build up a statistical distribution of spin configurations consistent with the data. A representative RMC fit is shown in Fig. 10, demonstrating good agreement between the model and the data.

We calculated the spin correlation function as defined in Eq. 5 for each of these fits, and then averaged all 100 to produce a final spin correlation function. We display this function, which is defined only for distances corresponding to Mn-Mn pairs, as a series of cyan arrows in Figure 7. The arrows represent the magnitude and net orientation (positive or negative) of the average correla-

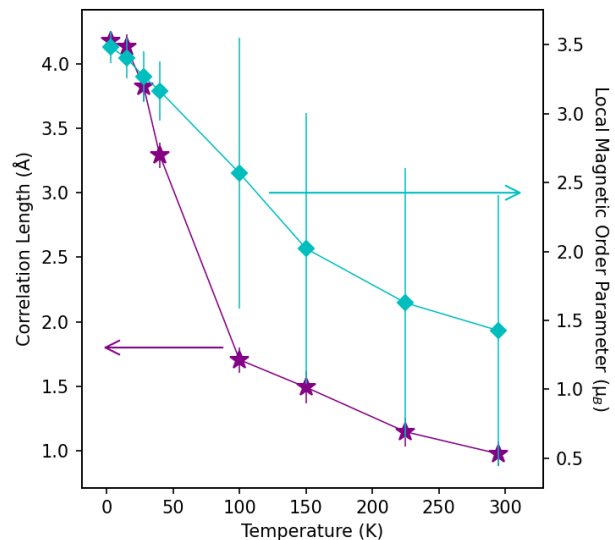


FIG. 9. Temperature dependence of the correlation length (left vertical axis) and locally ordered moment (right vertical axis) obtained from fits to d_{mag} .

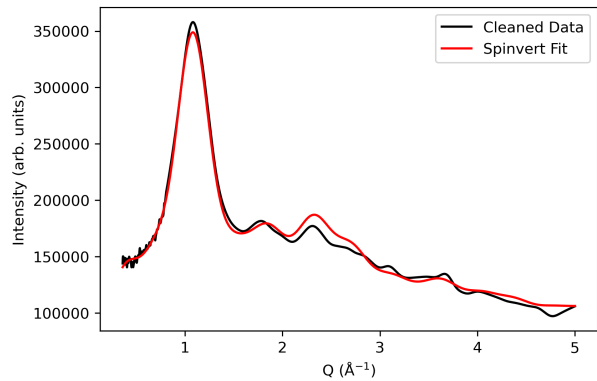


FIG. 10. RMC modeling of magnetic diffuse scattering data for $\text{Zn}_{0.5}\text{Mn}_{0.5}\text{Te}$ at 3 K, as carried out in Spinvert.

tion function at each Mn-Mn separation distance. The spin correlation function visualized in this way follows the shape of the mPDF data and fit quite well, confirming that the local magnetic correlations exhibit strong type-III character.

DISCUSSION AND CONCLUSION

The combined magnetometry, μSR , and neutron scattering results that we have presented highlight several notable features of the spin-glass transition in $\text{Zn}_{0.5}\text{Mn}_{0.5}\text{Te}$. Perhaps most striking is the observation that the instantaneous local magnetic configuration shows no significant change across the freezing temperature, as evidenced by the relative constancy of the diffuse magnetic scattering pattern in reciprocal space and corresponding mPDF pattern in real space. The frozen,

short-range-ordered type-III antiferromagnetic correlations that comprise the spin-glass state below T_f persist as dynamic correlations above T_f , with only a very gradual reduction of the magnetic correlation length and locally ordered magnetic moment as the temperature increases. The real-space mPDF data presented here emphasize this fact in a unique way. The direct determination of the magnetic correlation length ($\sim 5 \text{ \AA}$ at 3 K) and locally ordered magnetic moment ($\sim 3.4 \mu_B$ at 3 K) is likewise a unique aspect of the mPDF analysis.

Interestingly, because these energy-integrated neutron scattering measurements probe the instantaneous spin correlations, which do not change at the freezing temperature, the neutron experiment is essentially blind to the spin-glass transition. On the other hand, magnetometry and μSR show clear signs of the freezing transition, but at different temperatures: about 22 K for dc magnetometry, and between about 25 and 45 K for μSR . As mentioned previously, this apparent contradiction is resolved by noting the different time-scale sensitivities of these various techniques. For μSR , magnetic fluctuations slower than about 0.1 MHz appear static to the short-lived muons, whereas these fluctuations would still be too fast for dc magnetometry to detect. Upon approaching T_f from above, the spin fluctuations slow down gradually, first passing through the threshold to be perceived as static in the μSR experiment, and later becoming detectable by dc magnetometry at the actual freezing temperature. The observation that the apparent freezing transition as observed by μSR occurs over a relatively broad temperature window spanning about 20 K indicates that the spin fluctuation rate changes somewhat non-uniformly throughout the sample volume. Whether this is an intrinsic feature of dense spin glasses or a consequence of slight compositional inhomogeneities in the sample is an open question.

This work also introduces valuable technical developments for mPDF and diffuse scattering studies conducted on neutron instruments that are not specifically optimized for such experiments. Specifically, the data-cleaning algorithm to remove Bragg peaks and isolate diffuse scattering signals allows effective mPDF analysis even when the usual methods, such as generating the combined atomic and magnetic PDF by Fourier transforming both the nuclear and magnetic scattering together, cannot be used. These developments may significantly expand the range of experiments for which mPDF can be successfully applied.

Acknowledgements We thank the staff at TRIUMF and the High Flux Isotope Reactor for their valuable help and support during the experiments. The neutron and muon work was supported by the U.S. Department of Energy, Office of Science, Basic Energy Sciences (DOE-BES) through Award No. DE-SC0021134. A portion of this research used resources at the High Flux Isotope Reactor, a DOE Office of Science User Facility operated

by the Oak Ridge National Laboratory. The beam time was allocated to HB2A on proposal number IPTS-29767.

-
- [1] K. Binder and A. P. Young, Spin glasses: Experimental facts, theoretical concepts, and open questions, *Rev. Mod. Phys.* **58**, 801 (1986).
 - [2] J. A. Mydosh, Spin glasses: redux: an updated experimental/materials survey, *Rep. Prog. Phys.* **78**, 052501 (2015).
 - [3] C. Huang, Some experimental aspects of spin glasses: A review, *J. Magn. Magn. Mater.* **51**, 1 (1985).
 - [4] M. B. Weissman, What is a spin glass? A glimpse via mesoscopic noise, *Rev. Mod. Phys.* **65**, 829 (1993).
 - [5] C. M. Newman and D. L. Stein, Ordering and broken symmetry in short-ranged spin glasses, *J. Phys.: Condens. Mat.* **15**, R1319 (2003).
 - [6] D. L. Stein and C. M. Newman, *Spin glasses and complexity*, Vol. 4 (Princeton University Press, 2013).
 - [7] D. Meneghetti and S. S. Sidhu, Magnetic Structures in Copper-Manganese Alloys, *Phys. Rev.* **105**, 130 (1957).
 - [8] Y. J. Uemura, T. Yamazaki, D. R. Harshman, M. Senba, and E. J. Ansaldo, Muon-spin relaxation in AuFe and CuMn spin glasses, *Phys. Rev. B* **31**, 546 (1985).
 - [9] G. Ehlers, M. L. Crow, Y. Diawara, F. X. Gallmeier, X. Geng, G. E. Granroth, R. D. Gregory, F. F. Islam, R. O. Knudson, F. Li, M. S. Loyd, and B. Vacaliuc, Modern Trends in Neutron Scattering Instrument Technologies, *Instruments* **6**, 22 (2022).
 - [10] S. F. Parker, P. J. Baker, and R. McGreevy, A Vision for the Future of Neutron Scattering and Muon Spectroscopy in the 2050s, *ACS Phys. Chem. Au* **4**, 439 (2024).
 - [11] J. N. Graham, M. J. Coak, S. Son, E. Suard, J.-G. Park, L. Clark, and A. R. Wildes, Local nuclear and magnetic order in the two-dimensional spin glass $\text{Mn}_{0.5}\text{Fe}_{0.5}\text{PS}_3$, *Phys. Rev. Materials* **4**, 084401 (2020).
 - [12] Y. Zhang, T. Scholz, R. Dronskowski, M. T. McDonnell, and M. G. Tucker, Local magnetic cluster size identified by neutron total scattering in the site-diluted spin glass $\text{Sn}_x\text{Fe}_{4-x}\text{N}$ ($x = 0.88$), *Phys. Rev. B* **100**, 014419 (2019).
 - [13] Y. Li, P. G. LaBarre, D. M. Pajerowski, A. P. Ramirez, S. Rosenkranz, and D. Phelan, Neutron scattering study of fluctuating and static spin correlations in the anisotropic spin glass Fe_2TiO_5 , *Phys. Rev. B* **107**, 014405 (2023).
 - [14] P. G. LaBarre, D. Phelan, Y. Xin, F. Ye, T. Besara, T. Siegrist, S. V. Syzranov, S. Rosenkranz, and A. P. Ramirez, Fluctuation-induced interactions and the spin-glass transition in Fe_2TiO_5 , *Phys. Rev. B* **103**, L220404 (2021).
 - [15] T. M. Holden, G. Dolling, V. F. Sears, J. K. Furdyna, and W. Girit, Spin correlations in $\text{Zn}_{1-c}\text{Mn}_c\text{Te}$ alloys, *Phys. Rev. B* **26**, 5074 (1982).
 - [16] S. P. McAlister, J. K. Furdyna, and W. Girit, Magnetic susceptibility and spin-glass transition in $\text{Zn}_{1-x}\text{Mn}_x\text{Te}$, *Phys. Rev. B* **29**, 1310 (1984).
 - [17] J. K. Furdyna and N. Samarth, Magnetic properties of diluted magnetic semiconductors: A review (invited), *J. Appl. Phys.* **61**, 3526 (1987).
 - [18] P. M. Shand, A. D. Christianson, T. M. Pekarek, L. S. Martinson, J. W. Schweitzer, I. Miotkowski, and B. C. Crooker, Spin-glass ordering in the diluted magnetic

- semiconductor $\text{Zn}_{1-x}\text{Mn}_x\text{Te}$, Phys. Rev. B **58**, 12876 (1998).
- [19] K. Momma and F. Izumi, Vesta 3 for three-dimensional visualization of crystal, volumetric and morphology data, Journal of applied crystallography **44**, 1272 (2011).
- [20] B. A. Frandsen, X. Yang, and S. J. L. Billinge, Magnetic pair distribution function analysis of local magnetic correlations, Acta Cryst. A **70**, 3 (2014).
- [21] B. A. Frandsen and S. J. L. Billinge, Magnetic structure determination from the magnetic pair distribution function (mPDF): ground state of MnO, Acta Cryst. A **71**, 325 (2015).
- [22] A. Wiedenmann and P. Burlet, Spin Correlation in the Quasi-1D Spin Glass FeMgBO_4 , Solid State Commun. **38**, 129 (1981).
- [23] A. Wiedenmann, M. Hamedoun, and J. Rossat-Mignod, Short-range ordering in the spin glass system $\text{ZnCr}_2\text{Al}_{2-2x}\text{S}_4$, J. Phys. C: Solid State Phys. **18**, 2549 (1985).
- [24] A. S. Wills, G. S. Oakley, D. Visser, J. Frunzke, A. Harrison, and K. H. Andersen, Short-range order in the topological spin glass $(\text{D}_3\text{O})\text{Fe}_3(\text{SO}_4)_2(\text{OD})_6$ using *xyz* polarized neutron diffraction, Phys. Rev. B **64**, 094436 (2001).
- [25] G. Ehlers, J. E. Greedan, J. R. Stewart, K. C. Rule, P. Fouquet, A. L. Cornelius, C. Adriano, P. G. Pagliuso, Y. Qiu, and J. S. Gardner, High-resolution neutron scattering study of $\text{Tb}_2\text{Mo}_2\text{O}_7$: A geometrically frustrated spin glass, Phys. Rev. B **81**, 224405 (2010).
- [26] B. A. Frandsen and H. E. Fischer, A New Spin on Material Properties: Local Magnetic Structure in Functional and Quantum Materials, Chem. Mater. **36**, 9089 (2024).
- [27] B. A. Frandsen, K. A. Ross, J. W. Krizan, G. J. Nilsen, A. R. Wildes, R. J. Cava, R. J. Birgeneau, and S. J. L. Billinge, Real-space investigation of short-range magnetic correlations in fluoride pyrochlores $\text{NaCaCo}_2\text{F}_7$ and $\text{NaSrCo}_2\text{F}_7$ with magnetic pair distribution function analysis, Phys. Rev. Materials **1**, 074412 (2017).
- [28] E. Lefrançois, L. Mangin-Thro, E. Lhotel, J. Robert, S. Petit, V. Cathelin, H. E. Fischer, C. V. Colin, F. Damay, J. Ollivier, P. Lejay, L. C. Chapon, V. Simonet, and R. Ballou, Spin decoupling under a staggered field in the $\text{Gd}_2\text{Ir}_2\text{O}_7$ pyrochlore, Phys. Rev. B **99**, 060401 (2019).
- [29] Z. Dun, M. Daum, R. Baral, H. E. Fischer, H. Cao, Y. Liu, M. B. Stone, J. A. Rodriguez-Rivera, E. S. Choi, Q. Huang, H. Zhou, M. Mourigal, and B. A. Frandsen, Neutron scattering investigation of proposed Kosterlitz-Thouless transitions in the triangular-lattice Ising antiferromagnet TmMgGaO_4 , Phys. Rev. B **103**, 064424 (2021).
- [30] N. Qureshi, H. E. Fischer, S. X. M. Riberolles, T. C. Hansen, M. Ciomaga Hatnean, and O. A. Petrenko, Magnetic short-range order in polycrystalline SrGd_2O_4 and SrNd_2O_4 studied by reverse Monte Carlo simulations and magnetic pair-distribution function analysis, Phys. Rev. B **106**, 224426 (2022).
- [31] R. Baral, J. Christensen, P. Hamilton, F. Ye, K. Chesnel, T. D. Sparks, R. Ward, J. Yan, M. A. McGuire, M. E. Manley, J. B. Staunton, R. P. Hermann, and B. A. Frandsen, Real-space visualization of short-range antiferromagnetic correlations in a magnetically enhanced thermoelectric, Matter **5**, 1853 (2022).
- [32] B. A. Frandsen, R. Baral, B. Winn, and V. O. Garlea, Magnetic pair distribution function data using polarized neutrons and *ad hoc* corrections, J. Appl. Phys. **132**, 223909 (2022).
- [33] N. Roth, A. F. May, F. Ye, B. C. Chakoumakos, and B. B. Iversen, Model-free reconstruction of magnetic correlations in frustrated magnets, IUCrJ **5**, 410 (2018).
- [34] J. A. M. Paddison and A. L. Goodwin, Empirical Magnetic Structure Solution of Frustrated Spin Systems, Phys. Rev. Lett. **108**, 017204 (2012).
- [35] J. A. M. Paddison, J. R. Stewart, and A. L. Goodwin, Spinvert: a program for refinement of paramagnetic diffuse scattering data, J. Phys.: Condens. Mat. **25**, 454220 (2013).
- [36] T. Degen, M. Sadki, E. Bron, U. König, and G. Nénert, The HighScore suite, Powder Diffr. **29**, S13 (2014).
- [37] A. D. Hillier, S. J. Blundell, I. McKenzie, I. Umegaki, L. Shu, J. A. Wright, T. Prokscha, F. Bert, K. Shimomura, A. Berlie, H. Alberto, and I. Watanabe, Muon spin spectroscopy, Nat. Rev. Methods Primers **2**, 4 (2022).
- [38] K. A. Petersen, J. Black, and B. A. Frandsen, BEAMS: Basic and Effective Analysis for Muon spin Spectroscopy, <https://github.com/FrandsenGroup/beams> (2021).
- [39] K. Kodama, K. Ikeda, S.-i. Shamoto, and T. Otomo, Alternative Equation on Magnetic Pair Distribution Function for Quantitative Analysis, J. Phys. Soc. Jpn **86**, 124708 (2017).
- [40] B. A. Frandsen, H. K. Parker, J. A. Christensen, E. Stubben, and S. J. L. Billinge, diffpy.mpdf: open-source software for magnetic pair distribution function analysis, J. Appl. Cryst. **55**, 1377 (2022).
- [41] E. R. A. Fletcher, K. Higashi, Y. Kalcheim, H. Kageyama, and B. A. Frandsen, Uniform structural phase transition in V_2O_3 without short-range distortions of the local structure, Phys. Rev. B **104**, 184115 (2021).
- [42] J. A. Paddison, J. R. Stewart, and A. L. Goodwin, Spinvert: a program for refinement of paramagnetic diffuse scattering data, Journal of Physics: Condensed Matter **25**, 454220 (2013).
- [43] J. K. Furdyna, W. Giriat, D. F. Mitchell, and G. I. Sproule, The Dependence of the Lattice Parameter and Density of $\text{Zn}_{1-x}\text{Mn}_x\text{Te}$ on Composition, J. Solid State Chem. **46**, 349 (1983).
- [44] P. Burlet, E. Ressouche, B. Malaman, R. Welter, J. P. Sanchez, and P. Vulliet, Noncollinear magnetic structure of MnTe_2 , Phys. Rev. B **56**, 14013 (1997).
- [45] Y. Uemura, μSR relaxation functions in magnetic materials, in *Muon Science: Muons in Physics, Chemistry and Materials*, edited by S. Lee, R. Cywinski, and S. Kilscoy (Taylor & Francis, New York, 1999).
- [46] B. A. Frandsen, C. Read, J. Stevens, C. Walker, M. Christiansen, R. G. Harrison, and K. Chesnel, Superparamagnetic dynamics and blocking transition in Fe_3O_4 nanoparticles probed by vibrating sample magnetometry and muon spin relaxation, Phys. Rev. Materials **5**, 054411 (2021).
- [47] J. E. Pask, D. J. Singh, I. I. Mazin, C. S. Hellberg, and J. Kortus, Structural, electronic, and magnetic properties of MnO, Phys. Rev. B **64**, 024403 (2001).
- [48] R. Baral, A. V. Haglund, J. Liu, A. I. Kolesnikov, D. Mandrus, and S. Calder, Local spin structure in the layered van der Waals materials $\text{MnPS}_x\text{Se}_{3-x}$, Phys. Rev. B **110**, 014423 (2024).
- [49] T. Chatterji, Magnetic Structures, in *Neutron Scattering from Magnetic Materials*, edited by T. Chatterji (Elsevier Science, Amsterdam, 2006) Chap. 2, pp. 25–91.
- [50] L. M. Corliss, N. Elliott, and J. M. Hastings, Antifer-

romagnetic Structures of MnS_2 , MnSe_2 , and MnTe_2 , J. Appl. Phys. **29**, 391 (1958).

Supplementary Information: Determination of the Magnetic Structure of Spin Glass Compound $\text{Zn}_{0.5}\text{Mn}_{0.5}\text{Te}$ Using Real-Space Methods

Sabrina R. Hatt,¹ Camille Shaw,¹ Emma Zappala,¹ Raju Baral,^{1,2} Stuart Calder,² Gerald D. Morris,³ Brenden R. Ortiz,⁴ Karine Chesnel,¹ and Benjamin A. Frandsen¹

¹*Department of Physics and Astronomy,
Brigham Young University, Provo, Utah 84602, USA.*

²*Neutron Scattering Division, Oak Ridge National Laboratory, Oak Ridge, Tennessee 37831, USA.*

³*Centre for Molecular and Materials Science, TRIUMF,
Vancouver, British Columbia, Canada V6T 2A3*

⁴*Materials Science and Technology Division,
Oak Ridge National Laboratory, Oak Ridge, Tennessee 37831, USA.*

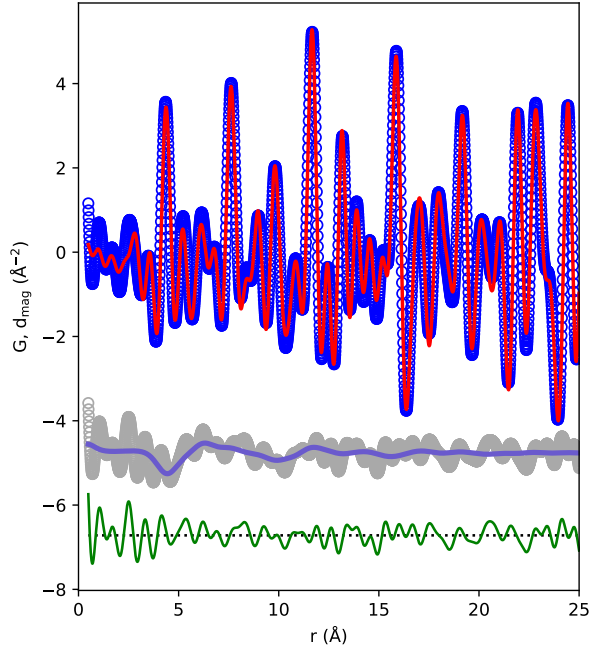


FIG. 1. Total PDF data for $\text{Zn}_{0.5}\text{Mn}_{0.5}\text{Te}$ at 3 K generated from the diffraction pattern collected with 1.12 \AA neutrons. The upper set of curves contains the experimental data (blue circles) and best-fit total PDF, comprised of the calculated atomic and magnetic PDF signals added together. Offset vertically below is the experimental mPDF signal in gray, obtained as the difference between the observed total PDF and the best-fit calculated atomic PDF, and the best-fit mPDF in purple. The overall fit residual is shown in green, further offset below.

We collected one diffraction pattern for $\text{Zn}_{0.5}\text{Mn}_{0.5}\text{Te}$ at 3 K using the short wavelength option ($\lambda = 1.12 \text{ \AA}$) at HB2A, yielding a larger maximum Q value of 9.8 \AA^{-1} than was available for the measurements using 1.54 \AA neutrons. After subtracting the instrumental background, we Fourier transformed the diffraction pattern to yield the total PDF, which includes both the nuclear (i.e. atomic) and magnetic PDF components. This total PDF pattern is shown by the blue symbols in Fig. 1. The limited Q range results in a very low-resolution atomic PDF which would not be suitable for investigating subtle details of the local atomic structure, but it is sufficient for our purpose of fitting a model of the known atomic structure and subtracting out the fitted atomic PDF component to isolate the mPDF component. The difference between the total PDF and the fitted atomic PDF is shown by the gray curve, offset below the overlaid blue and red curves. This gray curve represents the mPDF, together with any noise and systematic misfits from the atomic PDF model. Fitting a model of short-range-correlated type-III antiferromagnetism to the gray curve produces the purple calculated mPDF overlaid on the gray experimental mPDF signal. The model captures the overall

shape of the experimental curve quite well, indicating that we are performing a meaningful fit to the mPDF data. The high-frequency wiggles in the gray curve cannot be magnetic in origin, since the magnetic form factor restricts the magnetic scattering to relatively low Q and therefore low frequency in real space. The total PDF fit, consisting of the calculated best-fit nuclear PDF and mPDF, is shown by the red curve overlaid on the blue total PDF signal in Fig. 1. The overall fit residual is shown by the green curve offset below.

The local magnetic order parameter m , i.e. the magnitude of the correlated component of nearest-neighbor magnetic moments, can be calculated in units of μ_B as

$$m = gJ \sqrt{\frac{C_m \langle b \rangle^2}{C_a n_m}} \exp\left(\frac{-r_{NN}}{2\xi}\right), \quad (1)$$

where g is the Landè g-factor (2 in this case), J is the magnitude of the angular momentum vectors (i.e., spins) used in the calculation of the mPDF, C_m is the best-fit mPDF scale factor, C_a is the best-fit atomic PDF scale factor, $\langle b \rangle$ is the average nuclear scattering length of the material, n_m is the fraction of atoms in the material carrying a magnetic moment (0.25 in this case), r_{NN} is the distance separating nearest-neighbor spins, and ξ is the magnetic correlation length. Plugging the appropriate values into this equation yields $m = 3.4(3) \mu_B$ at 3 K. This was then used to calibrate the local magnetic order parameter values determined from the mPDF fits to the data collected with 1.54 Å neutrons, for which the atomic PDF could not be generated and therefore this method of comparing the atomic and magnetic scale factors could not be used.